

Fig. 3. Possible crystal structures of MgSiO_3 perovskite above 83 GPa. (A) $P2_1/m$ and (B) $Pmmn$. Projections along pseudo-cubic axes are shown for comparison. The crystal structures of $P2_1/m$ and $Pmmn$ have same tilting senses as $Pbnm$ and $P4_1/nmc$, respectively. The unit cell is shown by solid lines.

these technical improvements provide a better sample environment for examining the stability of MgSiO_3 perovskite and the structure of SiO_2 at extreme conditions.

Although two earlier quench studies (9, 11) and one in situ study (10) performed above 88 GPa reported the existence of MgSiO_3 perovskite, none of them reported the new diffraction feature we observed. Serghiou *et al.* (9) used Raman spectroscopy for phase identification on quenched samples. Because the phase transformation is expected to be subtle, the Raman study, which relied on only a few major Raman features, may not have been able to detect this change. Fiquet *et al.* (10) performed in situ angle-dispersive XRD measurements but their P-T conditions are generally lower than ours (Fig. 2). Andraut (11) studied aluminum- and iron-bearing MgSiO_3 perovskite samples that were heated for a few seconds. The lack of observation of new features in these studies indicates that further examination of possible perovskite structure is needed before any further conclusions can be drawn. The presence of a small but highly oriented unknown impurity phase can, for example, produce unexplained lines in an XRD pattern. Our observation that the new line is only rarely seen upon further heating of transformed perovskite samples indicates that preferred orientation and metastability may also be important factors.

The principal result of this study confirms the stability of $(\text{Mg,Fe})\text{SiO}_3$ perovskite to 2300-km depth conditions using in situ XRD measurements and homogeneous laser heating in both the radial and axial directions. It is also found that the structure of SiO_2 is the CaCl_2 type at pressures equivalent to 2400-km depth. Above 88 GPa, we observed the appearance of a new peak together with $Pbnm$ MgSiO_3 perovskite features. One possible explanation for this feature is transformation of $Pbnm$ perovskite to one of three other perovskite structures.

References and Notes

1. R. D. van der Hilst, H. Kárason, *Science* **283**, 1885 (1999).
2. T. Lay, Q. Williams, E. J. Garnero, *Nature* **392**, 461 (1998).
3. I. Sidorin, M. Gurnis, D. V. Helmberger, *Science* **286**, 1326 (1999).
4. L. H. Kellogg, B. H. Hager, R. D. van der Hilst, *Science* **283**, 1881 (1999).
5. E. Knittle, R. Jeanloz, *Science* **235**, 668 (1987).
6. C. Meade, H.-K. Mao, J. Hu, *Science* **268**, 1743 (1995).
7. S. K. Saxena *et al.*, *Science* **274**, 1357 (1996).
8. S. K. Saxena, L. S. Dubrovinsky, P. Lazor, J. Z. Hu, *Eur. J. Mineral.* **10**, 1275 (1998).
9. G. Serghiou, A. Zerr, R. Boehler, *Science* **280**, 2093 (1998).
10. G. Fiquet *et al.*, *Geophys. Res. Lett.* **27**, 21 (2000).
11. D. Andraut, *J. Geophys. Res.* **106**, 2079 (2001).
12. J. M. Brown, T. J. Shankland, *Geophys. J. R. Astron. Soc.* **66**, 576 (1981).
13. L. S. Dubrovinsky, S. K. Saxena, S. Rekh, *Science*, 13 August 1999 (www.sciencemag.org/cgi/content/full/285/5430/983a).
14. G. Serghiou, A. Zerr, R. Boehler, *Science*, 13 August 1999 (www.sciencemag.org/cgi/content/full/285/5430/983a).
15. K. J. Kingma, R. E. Cohen, R. J. Hemley, H.-K. Mao, *Nature* **374**, 243 (1995).
16. L. S. Dubrovinsky *et al.*, *Nature* **388**, 362 (1997).
17. L. S. Dubrovinsky *et al.*, *Chem. Phys. Lett.* **333**, 264 (2001).
18. D. Andraut, G. Fiquet, F. Guyot, M. Hanfland, *Science* **282**, 720 (1998).

19. N. C. Holmes, J. A. Moriarty, G. R. Gathers, W. J. Nellis, *J. Appl. Phys.* **66**, 2962 (1989).
20. L. W. Finger *et al.*, *Appl. Phys. Lett.* **39**, 892 (1981).
21. The laser-heating system (37) at GSECARS uses a TEM_{01} Nd:YLF laser, which provides a radially homogeneous temperature profile over 20 μm . Separate laser paths for each side of the sample reduces the axial thermal gradient, while separate imaging spectrometers enable us to measure the temperature profiles from both sides with a spatial resolution of 1.7 μm .
22. S.-H. Shim, T. S. Duffy, G. Shen, *J. Geophys. Res.* **105**, 25955 (2000).
23. A small horizontally focused x-ray beam was used (5 μm by 8 μm) to minimize the temperature inhomogeneity in the x-ray probed area. In order to reduce the effect of preferred crystallographic orientation at high temperature, the diamond anvil cell was oscillated by $\pm 20^\circ$ about its loading axis during the x-ray measurement. Alignment techniques ensured the co-linearity of the incident lasers, x-ray beam, and diamond cell rotation axis.
24. D. M. Teter, R. J. Hemley, G. Kresse, J. Hafner, *Phys. Rev. Lett.* **80**, 2145 (1998).
25. S. Speziale *et al.*, *J. Geophys. Res.* **106**, 515 (2001).
26. R. J. Hemley, C. T. Prewitt, K. J. Kingma, in *Silica: Physical Behavior, Geochemistry and Material Applications*, P. J. Heaney, C. T. Prewitt, G. V. Gibbs, Eds. (Mineralogical Society of America, Washington, DC, 1994), pp. 41–82.
27. A. M. Glazer, *Acta Crystallogr.* **B28**, 3384 (1972).
28. P. M. Woodward, *Acta Crystallogr.* **B53**, 32 (1997).
29. A. C. Larson, R. B. V. Dreele, Tech. Rep. LAUR 86-748, Los Alamos National Laboratory (1988).
30. B. Kiefer, L. Stixrude, *Eos* **81**, 555 (2000).
31. G. Shen, M. L. Rivers, Y. Wang, S. R. Sutton, *Rev. Sci. Instrum.* **72**, 1273 (2001).
32. Rhenium gasket lines arise from low-intensity ($\sim 1\%$) x-ray tails, which are completely removed by a secondary ("clean-up") slit system (37).
33. G. Fiquet *et al.*, *Phys. Earth Planet. Interiors* **105**, 21 (1998).
34. We thank S. Speziale and S. Shieh for experimental assistance, J. Akins and T. J. Ahrens for providing glass starting material, and P. M. Woodward and A. Kavner for helpful discussion. Supported by the NSF and the Packard foundation. Use of the Advanced Photon Source was supported by the DOE.

2 April 2001; accepted 17 August 2001

ENSO-like Forcing on Oceanic Primary Production During the Late Pleistocene

Luc Beaufort,¹ Thibault de Garidel-Thoron,¹ Alan C. Mix,² Nicklas G. Pisias²

Late Pleistocene changes in oceanic primary productivity along the equator in the Indian and Pacific oceans are revealed by quantitative changes in nanoplankton communities preserved in nine deep-sea cores. We show that variations in equatorial productivity are primarily caused by glacial-interglacial variability and by precession-controlled changes in the east-west thermocline slope of the Indo-Pacific. The precession-controlled variations in productivity are linked to processes similar to the Southern Oscillation phenomenon, and they precede changes in the oxygen isotopic ratio, which indicates that they are not the result of ice sheet fluctuations. The 30,000-year spectral peak in the tropical Indo-Pacific Ocean productivity records is also present in the Antarctica atmospheric CO_2 record, suggesting an important role for equatorial biological productivity in modifying atmospheric CO_2 .

Interannual variability of the thermocline depth is a characteristic feature of the equatorial Pacific Ocean that has a strong influ-

ence on oceanic primary production (1). Most of the time, the tropical trade winds transport surface waters westward. This lifts the ther-

REPORTS

mocline along the equator in the central and eastern Pacific but deepens the thermocline in the western Pacific, where warm surface waters pile up against the Australian and Asian continents. In the Indian Ocean, an analogous pattern exists but with a shallow thermocline in the west (the Somalian upwelling) and a deep thermocline in the east (2). When trade winds relax, the slope of

this basin-wide thermocline changes intensely. The thermocline rises in the western Pacific and in the eastern Indian Ocean, whereas it deepens on the other sides of these two basins [i.e., causing a typical El Niño–Southern Oscillation (ENSO) event in the Pacific]. Although the two oceans appear to be climatically independent of each other (2, 3), a synchronism of equatorial wind intensity has been observed between the Pacific and Indian oceans on decadal scales (4, 5). A shoaling of thermocline produces an increase in primary production. Thus, the ENSO-related thermocline slope variability has been

recognized as responsible for the “largest known natural perturbation of the global carbon cycle” on decadal scales (1). Here, we document long-term variations in the slope of the equatorial thermocline on the basis of patterns of changing primary productivity during the last two glacial cycles and its relation to global climate and orbital forcing.

We analyzed the coccolithophore community preserved in nine deep-sea cores taken from the tropical Indian and Pacific oceans (Fig. 1) (6). A precise chronology was obtained by tuning oxygen isotope records from foraminifera in most of the cores to the

¹CNRS-CEREGE, BP 80, 13545 Aix-en-Provence Cedex 04, France. ²College of Oceanography and Atmospheric Sciences, Oregon State University, Corvallis, OR 97331, USA.

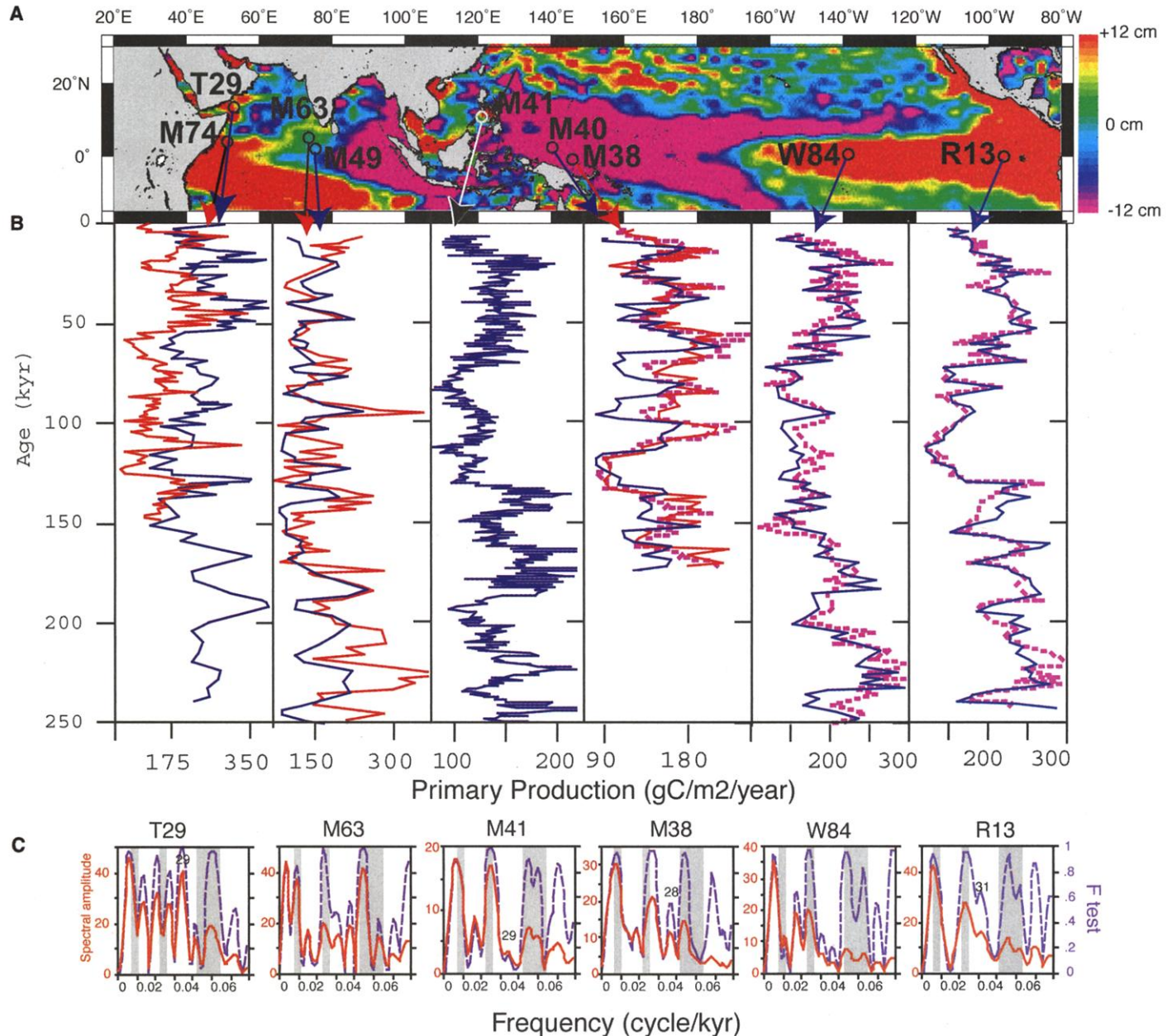
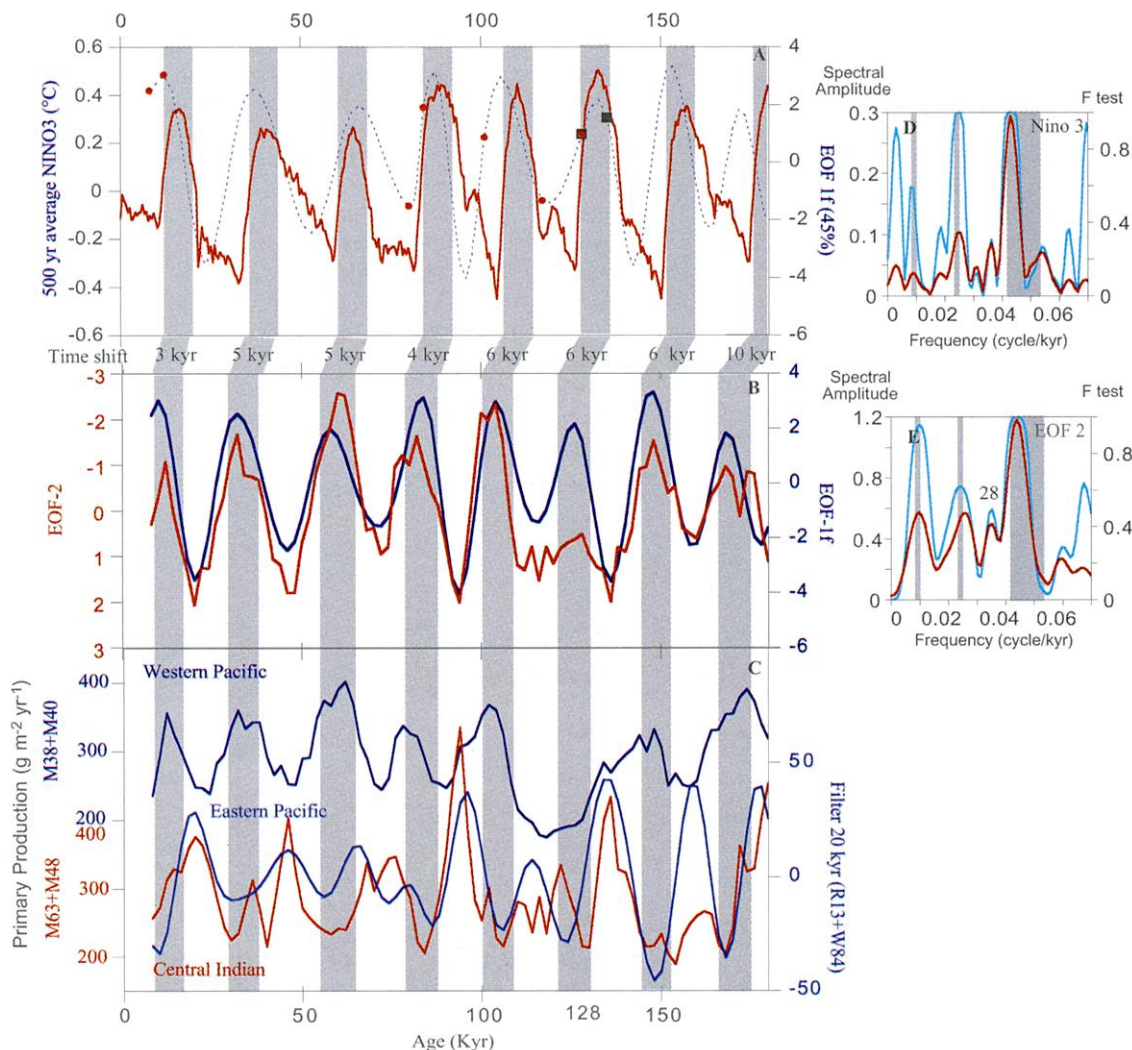


Fig. 1. (A) Map showing core locations and sea level anomalies relative to a 3-year mean recorded by Topex-Posidon during El Niño 1997 (cycle 193); scale is on the right. (B) Record of primary production from each core estimated on the basis of human (blue or red curves) and automated (neural network) counts (36)(dashed lines) of

coccoliths. (C) Spectral analysis (multitaper method) of ePP records. Amplitude spectra are in orange; the significance values of the peaks (*F* test) are in blue. Shaded areas indicate the orbital periods of 100, 41, and 23 to 19 ky. Significant peaks with a period of about 30 ky are also indicated.

Fig. 2. (A) The 500-year average NINO3 index from Zebiak-Cane model forced with Milankovitch solar variations (16) (solid red line). EOF-1 from the 20-ky bandpass-filtered ePP series (dashed blue line) with chronology based on U-Th date from Gallup *et al.* (19) (red dots) and Henderson and Slowey (20) (black squares). The data in (A) are shifted by 5 ky to match visual thermocline dynamics expressed in (B) and (C) (shaded areas correspond to high EOF-1f values). **(B)** EOF-2 from eight raw ePP records on reverted scale (red) and EOF-1 (EOF-1f) from the 20-ky bandpass-filtered ePP series (blue). **(C)** Productivity records added by pairs of cores: western Pacific (M38 added to M40 in dark blue), central Indian Ocean (M63 added to M48 in red), and eastern Pacific (20-ky filters of W84 added to 20-ky filter of core R13 in light blue). **(D and E)** Spectral analysis (multitaper method) of ENSO model (D) and EOF-2 (E). Amplitude spectra are in red; the significance values of the peaks (F test) are in light blue. Shaded areas indicate the orbital periods of 100, 41, and 23 to 19 ky.



SPECMAP stacked record (7) so that our sampling achieves a temporal resolution of 0.7 to 3 thousand years (ky). Six records span at least the last 240 ky, two shorter cores (M38 and M40) the last 180 ky, and one (M74) the last 150 ky. Most of the coccolithophore species live in near-surface waters where light for photosynthesis is abundant. Phytoplankton also requires nutrients, and thus thrives where a shallow thermocline brings subsurface nutrients into the upper euphotic zone. In contrast, the coccolithophore *Florisphaera profunda* lives in the deep-photoc zone, where nutrients are relatively abundant but light is rare (8). Where the thermocline is deep, total primary productivity is low, and the dominant coccolith species in fossil assemblages is *F. profunda* (9). As productivity increases, the relative abundance of *F. profunda* decreases. Thus, estimates of primary productivity (ePPs) are made from counts of the relative abundance of *F. profunda* (%Fp) (6, 10). The data are given as productivity estimates because, within tropical systems, productivity is highly correlated with the depths of the nutricline

and the thermocline (1, 11, 12).

The ePP records (Fig. 1) show large amplitude variability with regional similarities and contrasts that are explored using empirical orthogonal functions (EOFs). EOFs reduce the set of observations to a small number of spatiotemporal patterns (an EOF series) that can adequately describe the data (13, 14). It also provides statistics (loading) on how each original record contributes to the EOF series. Two significant EOF series (EOF-1 and EOF-2) have been extracted for the last 180 ky from the eight cores (Figs. 2, 3; the maximum duration represented by cores M38 and M40 is 180 ky). They describe 60% of the total variance in all eight cores. EOF-2 reflects a straightforward mechanism and is discussed first.

EOF-2 accounts for 19% of the total variance and opposes essentially the western Pacific with the central Indian Ocean (6), and it clearly fluctuates with the 23-ky cycle of Earth's precession (Fig. 2E). However, the eastern Pacific ePP records show weak precession cycles in comparison with the 41- and 100-ky cycles, and consequently they do not

contribute significantly to EOF-2. We repeated the EOF analyses on 23-ky bandpass-filtered ePP records. This filtering technique suppresses the influence of the large glacial-interglacial variability on the eastern Pacific productivity records. The first component of this new test (EOF-1f) approximates that of EOF-2, although it gives a much clearer picture of the opposition in dynamic between the western and eastern Pacific ePPs (Fig. 2) (6). This cyclic opposition can also be seen when comparing basin average regional records (Fig. 2C). Contemporary interannual variability in ENSO shows a similar spatial opposition in the altimetric anomaly (Fig. 1), thermocline depth, and hence productivity fluctuations in the equatorial Pacific (1) and equatorial Indian oceans (2). Thus, the opposition we found is likely to reflect similar variations in equatorial thermocline slope, although on a much longer time scale (15).

Interestingly, in every core analyzed, ePP records lead by about 2 ky the $\delta^{18}\text{O}$ records in the precession band (6). This lead indicates that insolation is the direct cause of ePP fluctuations, and that polar ice volume vari-

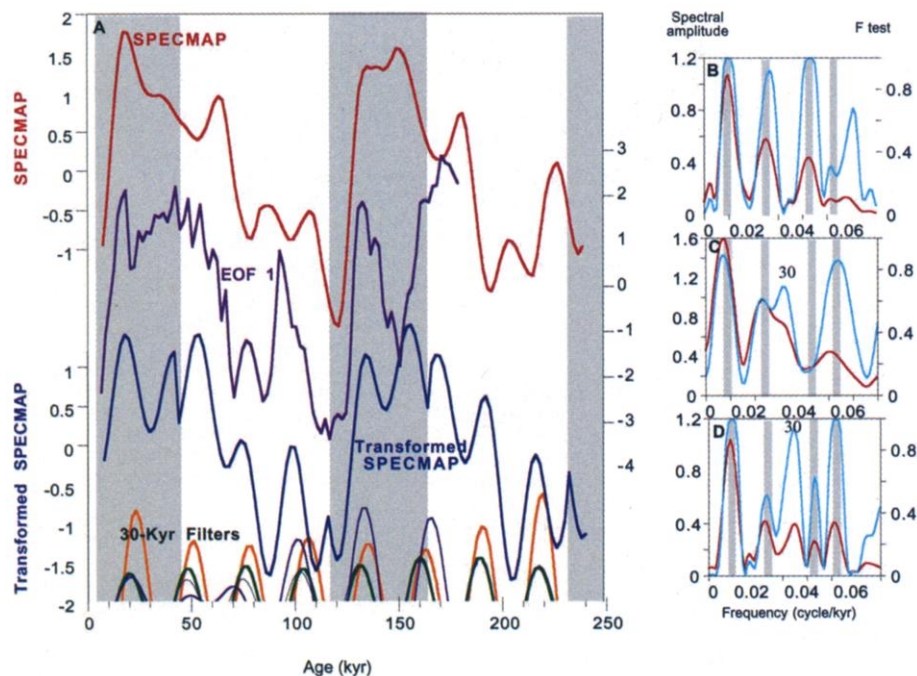


Fig. 3. (A) Purple line, first component of the EOF; red line, SPECMAP stack; blue line, SPECMAP stack transformed in the following manner: the stack was filtered at 100, 41, and 20 ky. The 20-ky filter was inverted for interglacial periods (unshaded areas) and kept as initial in glacial and during terminations (shaded area). The three filtered series were then added together. At the bottom positive part of 30-ky Gaussian filters (37) (centered on 0.034 ky^{-1} with a band width of 0.004 with cutting at period of 26.6 and 34.3 ky) of EOF (purple), transformed SPECMAP (blue), 23-ky sine-wave frequency modulated by 100- and 40-ky cycle from SPECMAP (green) (38), and $-\text{CO}_2$ from Vostok (orange) (30). (B to D) Spectral analysis (37) (multitaper method) of SPECMAP (B), EOF-1 (C), and transformed SPECMAP (D). Amplitude spectra are in red; the significance values of the peaks (F test) are in light blue. Shaded areas indicate the orbital periods of 100, 41, and 23 to 19 ky. The extra 30-ky period is also indicated.

ations ($\delta^{18}\text{O}$) do not significantly affect the low-latitude climate dynamics in that time scale. An ENSO modeling experiment over the past glacial-interglacial cycles has shown that changes in low-latitude insolation induce variations in the frequency and intensity of ENSO events (16). A very good agreement is found between the predictive ENSO model and EOF-2-1f time series, although an almost constant shift of about 5 ky occurs between the model and the EOFs (Fig. 2). This offset may partly be explained by the use of the SPECMAP chronology for our age model (7), because new radioisotope dates point to significantly older ages for most of the isotopic record than previously estimated [compare (17–20) with (7)]. Calibrating the $\delta^{18}\text{O}$ chronology based solely on the recent U/Th dates, the EOFs offer a better synchronism with the ENSO model (Fig. 2A). Although chronology is beyond the objective of this work, it appears that older ages in the SPECMAP chronology would reconcile model predictions and observed/measured data. Hence, the observed long-term variations of the equatorial thermocline slope would seem to be related to variations in the intensity of ENSO events driven by precession-related insolation changes.

EOF-1 accounts for 40% of the total variance. It characterizes productivity variations common to all sites (Fig. 3) (6). Because it contains significant periods close to the 100-ky (eccentricity) and 41-ky (obliquity) bands, and because EOF-1 broadly covaries with the SPECMAP stacked oxygen isotope record (Fig. 3), EOF-1 expresses the dominant influence of glacial variability on equatorial productivity. High EOF-1 values (i.e., high-productivity conditions) occur during maximum glacial conditions, low EOF-1 values (i.e., low-productivity conditions) during interglacial times. EOF-1 varies in phase with $\delta^{18}\text{O}$ in the eccentricity band and lags it in the obliquity band, indicative of a significant response of low-latitude productivity dynamics to glacial-interglacial variability. These spectral characteristics are shown by each ePP series (6), except the central Indian Ocean one (10). The process that increases primary production during glacial in the equatorial Indo-Pacific remains uncertain. It cannot correspond to an increase in the strength of zonal winds, because that would produce an increase of the slope of thermocline in the Pacific, a fact that is not observed for EOF-1 (6). Such a general rise of nutrient in the equatorial upper photic zone could be related

to a global increase of nutrient concentration in the intermediate waters that upwell into the photic zone. More likely it results from a weakened and/or shoaled stratification that permits an increased flux of new nutrients. A decrease of equatorial sea surface temperatures (14, 21, 22) relative to the intermediate water temperatures during glacial periods would weaken the stratification, and the thermocline would shoal (23). Dry weather conditions in the western Pacific (24) would further reduce stratification because a reduction of heavy rains would reduce fresh surface water inputs and its strong specific halocline. It has been shown that the global climate variability modulates the ENSO (23) by altering the background state and in particular the depth of the thermocline: Warmer climate increases the frequency and strength of the El Niño. The general fluctuations of the thermocline depth as recorded by EOF-1 are in complete agreement with those of the influence of the global climate on low-latitude oceanography.

Finally, the spectra of EOF-1, and to a lesser degree of EOF-2, reveal significant peaks at 30 and 19 ky (Figs. 2 and 3). These spectral peaks are interpreted as reflecting the phase modulation of precession in ePP: The time series of EOF-1 seems to be in phase with those of SPECMAP during maximum glacial and deglaciation (stripped in gray in Fig. 3A) conditions, but in anti-phase during interglacial periods. To illustrate this; we inverted the precession signal of the SPECMAP record for each interglacial period. The spectral signature of this new series (transformed SPECMAP, Fig. 3A) shows a distinct 30-ky period and a shift of the precession period from 23 ky to 19 ky (Fig. 3D). These spectral signatures are those of EOF-1. Therefore, the 30-ky component that occurs in EOF-1 as well as in most of the ePP series (Fig. 1) corresponds to a cyclic phase shift of the precession parameter. Two forcings are acting in phase opposition at a 20-ky time scale and in amplitude opposition at a 100-ky time scale. The mechanism involved is uncertain, but could be linked to the boreal summer monsoon (BSM) dynamics. Present climate studies show that the strengths of BSM and ENSO are often correlated with stronger BSMs during La Niña events [for example, (25)]. But on Milankovitch time scales, this is not the case: BSMs intensify during interglacial periods (26), whereas we have shown that ePPs (La Niña equivalent) increase during glacial periods. It is therefore plausible that during interglacials, intense BSMs somehow altered the path of the thermocline depth dynamics described above and were responsible for that 30-ky period.

A 30-ky period has been found in series from the tropical Pacific [see discussion in (14)] and tropical Indian (27–29) oceans, but so far not from the tropical Atlantic. We

speculate that the 30-ky cycle is restricted to the tropical Indo-Pacific Ocean (14), because the ENSO is characteristic of that area. However, the CO₂ record from the Vostok ice core also reveals a 30-ky cycle (30). Cross-spectral analyses indicate that the productivity series are highly coherent with the CO₂ record at the 30- and 23-ky periods, and that low CO₂ values are associated with high productivity (Fig. 3) (6). It is therefore possible that, with primary production acting as a significant sink in the carbon cycle, the 30-ky record in global CO₂ is the signature of ENSO-like control of biological production in the equatorial Indo-Pacific. This is consistent with a significant role of the low-latitude biological pump in controlling atmospheric CO₂ concentrations (31).

We have identified two independent forcings responsible for 60% of the long-term equatorial Indo-Pacific productivity dynamics. The first forcing concerns the response of the depth of the equatorial thermocline to global climatic variations. The second forcing is related to changes in the equatorial east-west thermocline tilt and is linked to the 23-ky period of Earth's precession. This precession-related variability could reflect the influence of low-latitude insolation on ENSO, as a predictive ENSO model stipulates (16). A similar dual "precession-glacial" forcing has been described recently on New Guinea corals (32). The 23-ky signal precedes ice volume variations by about 2 ky. Thus, long-term ENSO dynamics provide a possible causality for the growing body of evidence that low-latitude climates are early responders to orbital forcing (9, 10, 22, 33–35). Although minor, a 30-ky period is also evidenced. It is characteristic of the equatorial Indo-Pacific coherent with a similar period found in Vostok CO₂ record. That coherency attests to the importance of biological carbon fixation in the equatorial Indo-Pacific in controlling variations of atmospheric CO₂. Therefore, because of its early response and its possible effect on the carbon cycle, the 23-ky ENSO-like cycle is likely to have played a significant role in global climate dynamics.

References and Notes

1. D. Turk, M. J. McPhaden, A. J. Busalacchi, M. R. Lewis, *Science* **293**, 471 (2001).
2. P. J. Webster, A. M. Moore, J. P. Loschnigg, R. R. Leben, *Nature* **401**, 356 (1999).
3. N. H. Saji, B. N. Goswami, P. N. Vinayachandran, T. Yamagata, *Nature* **401**, 360 (1999).
4. C. D. Charles, D. E. Hunter, R. G. Fairbanks, *Science* **277**, 925 (1997).
5. J. E. Cole, R. B. Dunbar, T. R. McClanahan, N. A. Muthiga, *Science* **287**, 617 (2000).
6. Supplemental material is available at *Science* Online at www.sciencemag.org/cgi/content/full/293/5539/2440/DC1.
7. J. Imbrie et al., in *Milankovitch and Climate, Part 1*,

- A. L. Berger, J. Imbrie, J. D. Hays, G. Kukla, B. Saltzman, Eds. (Reidel, Dordrecht, Netherlands, 1984), vol. 1, pp. 269–305.
8. H. Okada, S. Honjo, *Deep Sea Res.* **20**, 355 (1973).
9. B. Molino, A. McIntyre, *Science* **249**, 766 (1990).
10. L. Beaufort et al., *Science* **278**, 1451 (1997).
11. M. R. Lewis, W. G. Harrison, N. S. Oakey, D. Herbert, T. Platt, *Science* **234**, 870 (1986).
12. We recognize that in some special cases (e.g., eastern Pacific), a shallow nutricline is a necessary but not a sufficient condition for high primary production. But this does not alter the broad picture that we describe in that paper.
13. A. C. Mix, W. F. Ruddiman, A. McIntyre, *Paleoceanography* **1**, 43 (1986).
14. N. G. Pisias, A. C. Mix, *Paleoceanography* **12**, 381 (1997).
15. The productivity record of Core M41 mimics those from the central and eastern Pacific. The effect of basin-wide thermocline tilt on productivity fluctuations in the Pacific has probably not been recorded in the Sulu Sea, because it is protected by the Philippine Islands and also because the PP dynamics is related to the winter monsoon.
16. A. C. Clement, R. Seager, M. A. Cane, *Paleoceanography* **14**, 441 (1999).
17. R. L. Edwards, J. H. Chen, T. L. Ku, G. J. Wasserburg, *Science* **236**, 1547 (1987).
18. E. Bard, B. Hamelin, R. G. Fairbanks, *Nature* **385**, 707 (1990).
19. C. D. Gallup, R. L. Edwards, R. G. Johnson, *Science* **263**, 796 (1994).
20. G. M. Henderson, N. C. Slowey, *Nature* **404**, 61 (2000).
21. A. C. Mix, A. E. Morley, N. G. Pisias, S. W. Hostetler, *Paleoceanography* **14**, 350 (1999).
22. D. W. Lea, D. K. Pak, H. J. Spero, *Science* **289**, 1719 (2000).

23. A. V. Fedorov, S. G. Philander, *Science* **288**, 1997 (2000).
24. J. R. Flenley, *Clim. Change* **39**, 177 (1998).
25. G. A. Meehl, *J. Clim.* **6**, 31 (1993).
26. W. L. Prell, in *Milankovitch and Climate, Part 1*, A. L. Berger, J. Imbrie, J. D. Hays, G. Kukla, B. Saltzman, Eds. (Reidel, Dordrecht, Netherlands, 1984), vol. 1, pp. 349–366.
27. S. Clemens, W. L. Prell, D. Murray, G. Shimmield, G. Weedon, *Nature* **353**, 720 (1991).
28. F. C. Bassinot et al., *Earth Planet. Sci. Lett.* **126**, 91 (1994).
29. G. J. Reichert, L. J. Lourens, W. J. Zachariasse, *Paleoceanography* **13**, 607 (1998).
30. J. R. Petit et al., *Nature* **399**, 429 (1999).
31. J. J. Rich, D. Hollander, G. E. Birchfield, *Global Biogeochem. Cycles* **13**, 531 (1999).
32. A. W. Tudhope et al., *Science* **291**, 1511 (2001).
33. E. M. Pokras, A. Mix, *Nature* **326**, 486 (1987).
34. J. Villanueva et al., *Paleoceanography* **13**, 561 (1998).
35. S. E. Harris, A. C. Mix, *Quat. Res.* **51**, 14 (1999).
36. D. Dollfus, L. Beaufort, *Neural Networks* **12**, 553 (1999).
37. D. Paillard, L. Labeyrie, P. Yiou, *Eos* **77**, 379 (1996).
38. The frequency modulation of precession by ice volume may be computed as $x_t = \cos(2\pi t/23.4) + \pi g_t/2$, where t is time and g_t is the modulating ice volume component (100 and 40 ky of SPECMAP varying between 0 and 1).
39. We thank IFRTF for financial and technical support for the Marion-Dufresne coring during IMAGES III cruise, Lamont-Doherty laboratory core repository for the samples from Core RC13-110, G. Ganssen for providing samples and stratigraphy from Core TY93-929, and M.-P. Aubry, L. Lourens, and two anonymous reviewers for reviewing an earlier version of the manuscript. Supported by NATO (L.B.) and by INSU ad hoc ocean and CNRS ECLIPSE grant (L.B.).

3 July 2001; accepted 22 August 2001

Embryonic Skulls of Titanosaur Sauropod Dinosaurs

Luis M. Chiappe,^{1*} Leonardo Salgado,² Rodolfo A. Coria³

Little is known about the cranial anatomy of the taxonomically diverse and geographically widespread titanosaurs, a paucity that has hindered inferences about the genealogical history and evolutionary development of the latest sauropod dinosaurs. Newly discovered fossil eggs containing embryonic remains from the Late Cretaceous of Argentina provide the first articulated skulls of titanosaur dinosaurs. The nearly complete fetal skulls shed light on the evolution of some of the most notable cranial features of sauropod dinosaurs, including the retraction of the external nares, the forward rotation of the braincase, and the abbreviation of the infraorbital region.

Chiappe et al. (1) reported embryonic remains of sauropod dinosaurs from incomplete skull remains from the Late Cretaceous nesting site of Auca Mahuevo (Patagonia, Argentina) (2). Six newly discovered eggs from this site containing exquisitely preserved skulls provide nearly complete and articulated cranial material of sauropod embryos (3, 4). The subtriangular skulls (Fig. 1) have large, circular orbits exceeding one-third of the cranial length. A large, triangular antorbital fenestra perforates the short snout, whose dorsal margin is slightly stepped. A tall premaxilla broadly sutures to a robust maxilla bearing slender and cylindrical teeth. The enamel of the tooth crowns is smooth and devoid of ser-

rations. The dentigerous portion of the maxilla occupies the rostral half of the element. The maxilla defines the rostral margin of a large ventral notch (Fig. 1A), which is caudally bound by the jugal and the quadratojugal. A similar large, ventral notch was reported for the Malagasy titano-

¹Department of Vertebrate Paleontology, Natural History Museum of Los Angeles County, 900 Exposition Boulevard, Los Angeles, CA 90007, USA. ²Museo de Geología y Paleontología, Universidad Nacional del Comahue, Buenos Aires 1400, (8300) Neuquén, Provincia del Neuquén, Argentina. ³Museo Carmen Funes, (8318) Plaza Huinca, Provincia del Neuquén, Argentina.

*To whom correspondence should be addressed. E-mail: lchiappe@nhm.org